PHYSICAL REVIEW D **92,** 084050 (2015)

Aligned spin neutron star-black hole mergers: A gravitational waveform amplitude model

Francesco Pannarale,[1,*] Emanuele Berti,[2,3,†] Koutarou Kyutoku,[4,‡] Benjamin D. Lackey,[5,6,§] and Masaru Shibata[7,¶]

[1]*School of Physics and Astronomy, Cardiff University, The Parade, Cardiff CF24 3AA, United Kingdom*
[2]*Department of Physics and Astronomy, The University of Mississippi, University, Mississippi 38677, USA*
[3]*CENTRA, Departamento de Física, Instituto Superior Técnico, Universidade de Lisboa, Avenida Rovisco Pais 1, 1049 Lisboa, Portugal*
[4]*Interdisciplinary Theoretical Science (iTHES) Research Group, RIKEN, Wako, Saitama 351-0198, Japan*
[5]*Department of Physics, Princeton University, Princeton, New Jersey 08544, USA*
[6]*Department of Physics, Syracuse University, Syracuse, New York 13244, USA*
[7]*Yukawa Institute for Theoretical Physics, Kyoto University, Kyoto 606-8502, Japan*

(Received 3 September 2015; published 22 October 2015)

The gravitational radiation emitted during the merger of a black hole with a neutron star is rather similar to the radiation from the merger of two black holes when the neutron star is not tidally disrupted. When tidal disruption occurs, gravitational waveforms can be broadly classified in two groups, depending on the spatial extent of the disrupted material. Extending previous work by some of us, here we present a phenomenological model for the gravitational waveform amplitude in the frequency domain encompassing the three possible outcomes of the merger: no tidal disruption, and "mild" and "strong" tidal disruption. The model is calibrated to 134 general-relativistic numerical simulations of binaries where the black hole spin is either aligned or antialigned with the orbital angular momentum. All simulations were produced using the SACRA code and piecewise polytropic neutron star equations of state. The present model can be used to determine when black-hole binary waveforms are sufficient for gravitational-wave detection, to extract information on the equation of state from future gravitational-wave observations, to obtain more accurate estimates of black hole-neutron star merger event rates, and to determine the conditions under which these systems are plausible candidates as central engines of gamma-ray bursts and macronovae/kilonovae.

DOI: 10.1103/PhysRevD.92.084050 PACS numbers: 04.25.dk, 97.60.Jd, 97.60.Lf, 04.30.-w

I. INTRODUCTION

The year 2015 will mark the beginning of the advanced gravitational-wave (GW) detector era. Exactly 100 years after Einstein formulated the theory of general relativity, the two Advanced Laser Interferometer Gravitational-Wave Observatory (LIGO) detectors [1,2] are about to start their observation runs. They will soon be followed by Virgo [3], and later on by the Kamioka gravitational wave detector (KAGRA) [4,5] and LIGO-India [6]. Detections will provide us with unprecedented information about astrophysical GW sources. Coalescing compact binary systems containing neutron stars (NSs) and/or black holes (BHs) are the main target for GW interferometric detectors. Their waveforms encode information about the masses, spins, distance, sky location, and orientation of the source, and, when NSs are present, about the NS equation of state (EOS). Detecting GWs emitted by compact binaries relies on matching noisy detector data with theoretical signal predictions and, therefore, requires us to build waveforms for the targeted sources that are as accurate as possible. At the same time, interpreting future observations calls for understanding as many details as possible about the sources.

In light of this, numerical relativity has made giant steps forward over the last decade, and simulations of the late inspiral and merger of compact binaries are now possible. As these calculations are resource intensive and time consuming, simulations that cover as many cycles as are necessary to fill the sensitivity bandwidth of the detectors and that span the whole parameter space are still beyond the reach of present-day computers. This is why semianalytical waveform models that fill the gap between perturbative methods—that describe the early inspiral stage—and numerical relativity are necessary. These models and numerical simulations are most advanced for BH-BH systems. Phenomenological inspiral-merger-ringdown (IMR) waveform models have been proposed for nonspinning binaries by Ajith *et al.* [7–9]; for spinning, nonprecessing binaries by Ajith *et al.* [10] and by Santamaría *et al.* [11], and more recently by Khan *et al.* [12,13]; and for spinning, precessing binaries by Hannam *et al.* [14]. These are generally referred to as "PhenomA," "PhenomB," "PhenomC," "PhenomD," and "PhenomP," respectively, and are all based on a post-Newtonian (PN) description of the early inspiral. Similarly, a lot of effort was

*francesco.pannarale@ligo.org
†eberti@olemiss.edu
‡koutarou.kyutoku@riken.jp
§bdlackey@syr.edu
¶mshibata@yukawa.kyoto-u.ac.jp

put into tuning the effective-one-body (EOB) model to BH-BH numerical simulations, and progress in this direction has been remarkable (see e.g. [15–21]). IMR models are employed in several contexts: to design and build GW detection templates at manageable computational costs (e.g. [22,23]), to test GW detection infrastructure (e.g. [24–26]), to evaluate statistical and systematic errors (e.g. [27,28]) and to perform detection rate calculations (e.g. [29–32]).

In the case of compact binaries containing at least one NS, the waveform modeling landscape is less developed, both because long and accurate simulations are particularly hard to achieve and because the parameter space is larger. The outcome and aftermath of NS-NS and NS-BH binary simulations (as opposed to BH-BH binaries) depend on several assumptions on physics that is currently underconstrained, including e.g. the NS EOS, the effect of magnetic fields and neutrino emission. This makes the NS-NS case particularly complex, as a hypermassive NS may form in the merger and oscillate for 10–100 milliseconds, emitting GWs in a fashion that is hard to predict from the parameters of the binary itself [33–35]. Due to this complex late stage of the evolution, attempts at constructing EOB-based waveform models valid up to merger [36] and possibly beyond [37,38] are still in their infancy. For NS-BH systems—the focus of this paper—one expects relatively large mass ratios, which cause complications at both the analytical and numerical level: the convergence of the analytical PN approximation is expected to be slower than for NS-NS systems [39], residual eccentricity in the initial data can be appreciable [40–42] (but see also [43,44]), and very different dynamical time scales must be tracked by numerical evolution codes [45–63].

Despite these obstacles, a clear picture of the GW emission of NS-BH binaries has emerged over the last few years. Most of the GW signal is emitted before the NS is tidally disrupted—if this happens at all—and before significant thermal effects occur. Furthermore, magnetic fields appear to barely affect GW emission [59]. These are particularly fortunate circumstances, as they imply that an ideal fluid-dynamics treatment with a cold EOS and an ideal-gas Γ-law for the thermal part are appropriate to simulate the dynamical regime that is of interest for the GW signal [51]. At least two papers attempted a phenomenological description of the GWs emitted by NS-BH binaries.

In the first paper, Lackey *et al.* [64] developed an analytic representation of the NS-BH IMR waveform calibrated to 134 numerical waveforms produced by the SACRA code [65] with the main goal of assessing the measurability of the NS tidal deformability.

A subset of these simulations for systems with nonspinning BHs was then used in work by Pannarale *et al.* [66] (henceforth Paper I) to obtain a phenomenological NS-BH IMR waveform *amplitude* model in the frequency domain. This model was, at heart, a "distortion" of the PhenomC BH-BH model. Paper I paid particular attention to the accuracy of the GW spectrum at high frequencies—where the EOS-related phenomenology takes place—and to the determination of a cutoff frequency in the GW emission. This cutoff frequency is especially important in the construction of NS-BH template banks. If a BH-BH-like template built to detect a disruptive NS-BH coalescence were to be truncated at a frequency that is too low with respect to the physical cutoff frequency of the source, a loss in recovered signal-to-noise ratio would occur. If on the other hand the truncation frequency were to be increased in order to counteract this problem, it could become too high with respect to the physical cutoff frequency of the NS-BH source, and this would possibly result in penalizing the template by degrading its performance in chi-square tests, which would also be detrimental to the detection.

The goal of the present paper is to extend the work of Paper I to NS-BH systems with a nonprecessing, spinning BH, using the full set of 134 hybrid waveforms considered in [64]. The phenomenological model based on this catalog allows us to produce the most accurate determination of cutoff frequencies for NS-BH GW signals, with relative errors on the cutoff frequency below 10%. These errors are well below the errors one would obtain using either BH-BH models or the NS-BH model of [64], with immediate applications in setting up template banks to target these systems. As for Paper I, we adopt a conservative approach and focus on the analytical modeling of the GW *amplitude* in the frequency domain, because residual eccentricity in our initial data and the short duration of our simulations do not guarantee an accurate phasing in the whole parameter space; see Hannam *et al.* [67] for how mass ratio affects the minimum number of numerical waveform cycles necessary to ensure an accurate phase and amplitude modeling, and [64] for issues in building hybrid waveforms for NS-BH binaries.

The plan of the paper is as follows. In Secs. II and III we review the basics of the numerical simulations and gravitational waveform hybrids, respectively, used to build and test the phenomenological model discussed in this paper. In Sec. IV we describe the waveform model for NS-BH binaries with a spinning BH. In Sec. V we compare our model against numerical data. Section VI discusses some important applications of our model, in particular predictions for the tidal disruption frequency and their implications for GW detection and the modeling of short gamma-ray bursts (SGRBs). Finally, in Sec. VII we summarize our conclusions and point out directions for future work. Throughout the paper, unless otherwise noted, we use geometrical units ($G = c = 1$).

II. THE NUMERICAL SIMULATIONS

Our phenomenological models are calibrated to and tested against the gravitational waveforms used in [64]. The waveforms are derived by numerical-relativity

simulations performed by the SACRA adaptive-mesh refinement code [65]. The details of the code are described in [47]. Here we only briefly discuss the key differences with respect to the simulations performed to derive the waveforms used in Paper I. Binaries in quasiequilibrium states are prepared as initial conditions for the simulations using the multidomain spectral method library LORENE [68]. In this work we allow the BHs to have nonzero spins aligned with the orbital angular momentum of the binary. The formulation and numerical methods for computing quasiequilibrium configurations are the same as in [69], except for the implementation of BH spins [47]. Gravitational waveforms are computed from the Weyl scalar Ψ_4 by integrating twice in time using a so-called fixed-frequency integration method [70] to filter out unphysical low-frequency components (see also [64,71]).

We adopt piecewise polytropic EOSs, which mimic nuclear-theory-based EOSs with a small number of parameters [72], to model the NS matter at zero temperature. Each piecewise polytrope is characterized by polytropic constants κ_i and adiabatic indices Γ_i as

$$P(\rho) = \kappa_i \rho^{\Gamma_i} \quad \text{for } \rho_{i-1} \leq \rho < \rho_i \quad (i = 1\ldots, n), \tag{1}$$

where ρ and P are the rest-mass density and pressure, respectively. At the critical densities ρ_i we further require the pressure to be continuous, i.e.

$$\kappa_i \rho_i^{\Gamma_i} = \kappa_{i+1} \rho_i^{\Gamma_{i+1}}, \tag{2}$$

and the EOS is thus completely specified by κ_1, Γ_i, and ρ_i $(i = 1\ldots, n)$. In this work, we adopt the same piecewise polytropes that were adopted in Paper I and in [64]. More specifically, n is set to be 2, the parameters $\{\kappa_1, \Gamma_1\}$ for the low-density crust regions are fixed, and the two parameters Γ_2 and $P_{\rm fidu} \equiv P(\rho = 10^{14.7}\ {\rm g/cm^3})$ are systematically varied to span a plausible range of nuclear-matter properties. In the dynamical simulations, thermal corrections are added in an ideal-gas-like form in order to capture the effect of shock heating [46,47].

The 134 NS-BH simulations used in this paper are listed in Table II of [64]. The mass ratio $Q \equiv M_{\rm BH}/M_{\rm NS}$ spans the values $\{2, 3, 4, 5\}$ and the BH dimensionless spin parameter χ takes the values $\{-0.5, 0, 0.25, 0.5, 0.75\}$. We adopt $\chi = -0.5$ only for $Q = 2$, because the combination of negative χ and large Q (say ≥ 3) yields small tidal effects during the coalescence. The NS mass $M_{\rm NS}$ is set to $1.35M_\odot$ for all the runs, with the exception of some $(Q, \chi) = (2, 0.75)$ and (2,0) cases, in which $M_{\rm NS}$ can also take the values $\{1.20M_\odot, 1.45M_\odot\}$ and $1.45M_\odot$, respectively. The EOSs are the same 21 models used in Paper I and [64] (see Fig. 1 therein for a representation in the piecewise polytropic EOS parameter space) and Fig. 1 in [46] for the NS equilibrium sequences yielded by these EOSs). For all combinations of Q and χ with $M_{\rm NS} = 1.35M_\odot$, the runs are performed adopting EOSs with $\Gamma_2 = 3.0$; additionally, EOSs with $\Gamma_2 = 2.4$, 2.7, and 3.3 are employed for models with $(Q, \chi) = (2, 0)$, (3,0.5), and (5,0.75).

To build and test our phenomenological NS-BH waveform model we use the hybrid waveforms of [64], which are also based on the numerical-relativity simulations just described (see next section). As in Paper I, we divide the data sets into two groups: one to build the waveform model and one to test it. In the simulations used to build the model the NS mass is $M_{\rm NS} = 1.35M_\odot$, and we use the $\Gamma_2 = 3.0$ EOSs denoted by 2H, H, HB, and B with $\log(P_{\rm fidu}/({\rm dyne/cm^2})) = 34.9$, 34.5, 34.4, and 34.3, respectively (see, for example, Paper I for this nomenclature): these are 59 data sets. The remaining 75 cases are not used to tune the waveform model, but just to test it.

III. THE HYBRID WAVEFORMS

In order to build our phenomenological NS-BH frequency-domain waveform amplitude model, we must first construct accurate IMR waveforms. This is done by matching each of the numerical NS-BH waveforms described in the previous section—which all begin ∼10 GW cycles before merger—to an inspiral waveform model, and by then splicing them together. We use the PhenomC BH-BH model of [11] as our inspiral waveform—a sound approximation, as tidal effects on the amplitude are negligible in this stage—and, unless otherwise noted and in accordance with the conventions of [11], all frequencies in this section and in the rest of the paper are to be intended as multiplied by the sum $m_0 = M_{\rm NS} + M_{\rm BH}$ of the two initial masses; i.e. we use units in which $m_0 = 1$. Similarly, times are to be intended as divided by m_0.

When matching waveforms, a time constant τ and phase constant ϕ are the two free parameters that need to be fixed. For a generic waveform $h(t)$, the time and phase can be adjusted to produce a shifted waveform $h^{\rm shift}(t; \tau, \phi) = h(t - \tau)e^{i\phi}$. The Fourier-transformed waveform,[1] which can be written in terms of amplitude and phase as $h(f) = A(f)e^{i\Phi(f)}$, has a corresponding shifted waveform $h^{\rm shift}(f; \tau, \phi) = A(f)e^{i\Phi^{\rm shift}(f;\tau,\phi)}$, where $\Phi^{\rm shift}(f; \tau, \phi) = \Phi(f) + 2\pi f\tau + \phi$. Because the time and phase constants have no impact on the GW amplitude in the frequency domain, we do not need to calculate them in this work, where we only model the amplitude $A(f)$.

Although the time and phase constants do not impact the amplitude, there is still some freedom in constructing the hybrid. We will use the method of Lackey *et al.* [64]. In the time domain, the numerical waveform begins with a finite amplitude, leading to the oscillatory Gibbs phenomenon that results from Fourier transforming a waveform segment with nonzero starting amplitude. We

[1]We omit the tilde over Fourier-transformed quantities in order to keep the notation lighter, as $h(t)$ will no longer appear in the rest of the paper.

therefore begin by windowing the numerical NS-BH waveform with a Hann window over the interval w_i to w_f (of width $w_f - w_i$) defined as

$$w_{\rm on}(t) = \frac{1}{2}\left[1 - \cos\left(\frac{\pi[t - w_i]}{w_f - w_i}\right)\right]. \tag{3}$$

We set the start of the window to be the start of the numerical waveform at $w_i = 0$ and use a width of 300 by setting $w_f = 300$, as in Ref. [64].

We are also free to choose the frequency interval for splicing the numerical waveform onto the analytic, inspiral waveform. This interval should be at high enough frequencies to exclude the effects of windowing at the beginning of the numerical waveform. It should also exclude the small initial eccentricity ($e_0 \sim 0.03$) that dies down after a few orbits and results from providing the numerical simulation with quasicircular (zero radial velocity) initial conditions that ignore the small radial velocity due to GW radiation reaction. However, the splicing interval should also be at a frequency that is low enough to capture the matter effects, present in the numerical simulations, that take place just before merger. We smoothly turn on the numerical waveform and smoothly turn off the analytic, inspiral waveform within a splicing window $s_i < f < s_f$ using Hann windows:

$$w_{\rm off}(f) = \frac{1}{2}\left[1 + \cos\left(\frac{\pi[f - s_i]}{s_f - s_i}\right)\right], \tag{4}$$

$$w_{\rm on}(f) = \frac{1}{2}\left[1 - \cos\left(\frac{\pi[f - s_i]}{s_f - s_i}\right)\right]. \tag{5}$$

The amplitude of the hybrid waveform is then

$$A_{\rm hybrid}(f) = \begin{cases} A_{\rm BBH}(f), & f \le s_i, \\ w_{\rm off}(f)A_{\rm BBH}(f) + w_{\rm on}(f)A_{\rm NR}(f), & s_i < f \le s_f, \\ A_{\rm NR}(f), & f > s_f. \end{cases} \tag{6}$$

As in Ref. [64], we use a starting frequency of $s_i = 0.018$ and an ending frequency of $s_f = 0.019$.

IV. MODELING SPINNING NEUTRON STAR-BLACK HOLE WAVEFORMS

In this section we provide a detailed description of our phenomenological model for the frequency-domain GW amplitude of nonprecessing NS-BH binaries with a spinning BH component. This new model generalizes the model presented in Paper I for nonspinning binaries; throughout the discussion we will point out differences with respect to the formulation reported in Paper I.

In accordance with the simulations and hybrid waveforms at our disposal, we set the BH spin vector to be aligned to the orbital angular momentum of the binary. Additionally, we use the notation $w^{\pm}_{f_0,d}(f)$ for the windowing functions

$$w^{\pm}_{f_0,d}(f) \equiv \frac{1}{2}\left[1 \pm \tanh\left(\frac{4(f - f_0)}{d}\right)\right] \tag{7}$$

centered in f_0 with width d.

Before discussing the waveform model itself, we must introduce two reference GW frequencies: these are $f_{\rm tide}$ and $f_{\rm RD}$. The former is the GW frequency at the *onset* of the NS tidal disruption, while the latter is the dominant ($\ell = m = 2$, $n = 0$) ringdown frequency of the remnant BH. The BH remnant dominant ringdown frequency $f_{\rm RD}$ depends on the mass $M_{\rm f}$ and spin parameter $\chi_{\rm f}$ of the BH remnant of the NS-BH merger. These are calculated according to the model discussed in [73,74], while the fitting formulas that relate $\chi_{\rm f}$ and $M_{\rm f}$ to $f_{\rm RD}$ are provided in [75]. To compute $f_{\rm tide}$, on the other hand, one must first determine a coefficient $\xi_{\rm tide}$ that provides a relativistic correction to the standard Newtonian estimate of the orbital radius at *mass shedding* [76]. This coefficient can be found by solving the equation

$$\frac{M_{\rm NS}\xi^3_{\rm tide}}{M_{\rm BH}} = \frac{3[\xi^2_{\rm tide} - 2\mu\xi_{\rm tide} + \mu^2\chi^2]}{\xi^2_{\rm tide} - 3\mu\xi_{\rm tide} + 2\chi\sqrt{\mu^3\xi_{\rm tide}}}, \tag{8}$$

where $\mu = M_{\rm BH}/R_{\rm NS} = Q\mathcal{C}$, with $\mathcal{C} = M_{\rm NS}/R_{\rm NS}$ denoting the NS compactness. The orbital radius at mass shedding is now given by

$$\tilde{r}_{\rm tide} = \xi_{\rm tide}R_{\rm NS}(1 - 2\mathcal{C}). \tag{9}$$

The tidal frequency $f_{\rm tide}$ then reads

$$f_{\rm tide} = \pm\frac{1}{\pi\left(\chi_{\rm f}M_{\rm f} + \sqrt{\tilde{r}^3_{\rm tide}/M_{\rm f}}\right)}, \tag{10}$$

where upper/lower signs hold for prograde/retrograde orbits. So far—aside from the inclusion of χ-dependent terms in Eqs. (8)–(10) and in obtaining $M_{\rm f}$ and $\chi_{\rm f}$ from the model of [73,74]—nothing differs from the approach laid out in Paper I. We would like to note that in the process of calculating $\chi_{\rm f}$ and $M_{\rm f}$ one must also determine another quantity that plays a role in the gravitational waveform model. This is the mass of the torus that may remain around the BH at late times, $M_{\rm b,torus}$, modeled using the fitting formula [76]

$$\frac{M_{\rm b,torus}}{M_{\rm b,NS}} = \frac{0.296\tilde{r}_{\rm tide} - 0.171r_{\rm ISCO}}{R_{\rm NS}}, \tag{11}$$

where $M_{\rm b,NS}$ is the rest mass of the NS in isolation and $r_{\rm ISCO}$ is the radius of the innermost stable circular orbit (ISCO) of the initial BH in isolation [77]:

$$\bar{r}_{\rm ISCO} = [3 + Z_2 \mp \sqrt{(3-Z_1)(3+Z_1+2Z_2)}],$$
$$Z_1 = 1 + (1-\chi^2)^{1/3}[(1+\chi)^{1/3} + (1-\chi)^{1/3}],$$
$$Z_2 = \sqrt{3\chi^2 + Z_1^2}. \quad (12)$$

As in Paper I, we write the amplitude $A_{\rm Phen}(f)$ of the frequency-domain signal $h_{\rm Phen}(f) = A_{\rm Phen}(f)e^{i\Phi_{\rm Phen}(f)}$ as a sum of three terms:

$$A_{\rm Phen}(f) = A_{\rm PN}(f) w^-_{\epsilon_{\rm ins}\tilde{f}_0, d+\sigma_{\rm tide}} + 1.25\gamma_1 f^{5/6} w^-_{\tilde{f}_0, d+\sigma_{\rm tide}} + \mathcal{A}_{\rm RD}(f) w^+_{\tilde{f}_0, d+\sigma_{\rm tide}}, \quad (13)$$

where $A_{\rm PN}(f)$ is the inspiral contribution, based on the stationary-phase approximation and obtained by combining a 3PN-order time-domain expansion of the amplitude and the TaylorT4 description for the phase (see [11] for further details); the second term models the premerger and merger (strong-field) modifications to the PN inspiral (the γ_1 coefficient is provided, once more, in [11]); and $\mathcal{A}_{\rm RD}$ is the ringdown amplitude. This is modeled via a Lorentzian $\mathcal{L}(f, f_0, \sigma) \equiv \sigma^2/[(f-f_0)^2 + \sigma^2/4]$:

$$\mathcal{A}_{\rm RD}(f) = \epsilon_{\rm tide}\delta_1 \mathcal{L}(f, f_{\rm RD}(\chi_{\rm f}, M_{\rm f}), \delta_2' f_{\rm RD}/\mathcal{Q}(\chi_{\rm f})) f^{-7/6}, \quad (14)$$

where[2] δ_1 is the ringdown amplitude fitted to BH-BH hybrid waveform data in [11]; $\epsilon_{\rm tide}$ is an NS-BH correction discussed later on in this section; and δ_2' is a fudge factor which accounts for errors in the model used to compute $\chi_{\rm f}$, as this spin parameter is in turn used to determine the quality factor $\mathcal{Q}$ of the BH remnant (once again via the fitting formulas of [75]). We note that the PhenomC model also uses a fudge factor, δ_2, but $\chi_{\rm f}$ is determined using the formulas in [78]. Therefore, rather than correcting the PhenomC parameter δ_2 as we did in Paper I, in this paper we introduce a δ_2' parameter in order to disentangle PhenomC and our model more clearly. The remaining elements of Eq. (13) to be discussed are the windowing functions. As for the PhenomC model, d is set to 0.015, but, just as in Paper I, we allow for a correction $\sigma_{\rm tide}$ to the width, we do not necessarily tie the central windowing frequencies to the BH remnant ringdown frequency, and we do not always fix the central windowing frequencies of the first two terms in $A_{\rm Phen}(f)$ ($\epsilon_{\rm ins}\tilde{f}_0$ and $\tilde{f}_0$, respectively) to the same value. More details on how $\sigma_{\rm tide}$, $\epsilon_{\rm ins}$ and $\tilde{f}_0$ are determined are given further on in this section.

To summarize, in order to build $A_{\rm Phen}(f)$ given $M_{\rm BH}$, χ, $M_{\rm NS}$ and an EOS (which determines the NS radius $R_{\rm NS}$ and its baryonic rest mass $M_{\rm b,NS}$), one must begin by computing (1) γ_1 and δ_1 according to [11]; (2) $M_{\rm b,torus}$ using Eqs. (11)–(12); (3) $M_{\rm f}$ and $\chi_{\rm f}$ following the model reported in [73,74]; (4) $f_{\rm RD}(M_{\rm f}, \chi_{\rm f})$ and $\mathcal{Q}(\chi_{\rm f})$ via the fits of [75]; and (5) $f_{\rm tide}$, following Eqs. (8)–(9). At this point the model splits into four cases, depending on the values of $f_{\rm tide}$, $f_{\rm RD}$, and $M_{\rm b,torus}$. These cases reflect the different phenomenology of NS-BH binary mergers observed in the 59 simulations used to build the model (see Sec. II): "disruptive," "nondisruptive," and "mildly disruptive" with and without a torus remnant.

Before laying out the necessary details about the four alternative waveforms in the remaining subsections, we will briefly explain how the four phenomenological models were obtained. Each of the hybrid waveform amplitudes corresponding to nondisruptive mergers—out of the 59 hybrids used to build our model—was fitted with the *ansatz* in Eq. (15) below, leaving $\epsilon_{\rm tide}$, $\sigma_{\rm tide}$, and δ_2' as free coefficients. The values of the free coefficients were then themselves fitted as detailed in Eqs. (16)–(20). The same procedure was followed for the disruptive mergers, where, this time, the waveform amplitude *ansatz* is given in Eq. (21) and the values of the free coefficients $\epsilon_{\rm ins}$ and $\sigma_{\rm tide}$ are fitted with Eqs. (22)–(25). All equations involved in this process were inspired by the nonspinning study reported in Paper I. For the two mildly disruptive cases, we adopted a strategy that is similar to the one discussed in Paper I: we picked and combined ingredients from disruptive and nondisruptive phenomenological waveforms, without having to perform additional fits.

A. Nondisruptive mergers

If $f_{\rm tide} \geq f_{\rm RD}$ and $M_{\rm b,torus} = 0$, the merger is nondisruptive. Notice that the first condition differs slightly from the one used in the nonspinning waveform model reported in Paper I. Additionally, we had not explicitly required the second condition in Paper I, because we never encountered nonspinning cases for which the analytical models would predict $M_{\rm b,torus} > 0$ and $f_{\rm tide} > \tilde{f}_{\rm RD} \equiv 0.99 \times 0.98\, f_{\rm RD}$. For nondisruptive mergers the binary can complete its full inspiral stage, and therefore we set $\epsilon_{\rm ins} = 1$ in Eq. (13). Moreover, the BH remnant ringdown is excited, so the windowing functions in Eq. (13) can be centered around $\tilde{f}_0 = \tilde{f}_{\rm RD}$.[3] $A_{\rm Phen}(f)$ thus takes the form

[2] The third argument here corrects a typo in Eq. (3) of Paper I.

[3] Nondisruptive NS-BH mergers essentially behave as BH-BH mergers. In PhenomC waveforms, $\tilde{f}_0$ is set to $0.98 f_{\rm RD}$; this quantity in turn depends on the mass of the BH remnant, which is set to the sum of the individual masses of the binary components, m_0. In our model the mass of the BH remnant is instead determined with the approach described in [73]. More specifically, $M_{\rm f}$ is always smaller than m_0, the final mass choice made in PhenomC. This increases $f_{\rm RD}$; hence the need for the extra 0.99 in our definition of $\tilde{f}_0$.

$$A_{\rm Phen}(f) = A_{\rm PN}(f) w^{-}_{\tilde{f}_{\rm RD}, d+\sigma_{\rm tide}} + 1.25\gamma_1 f^{5/6} w^{-}_{\tilde{f}_{\rm RD}, d+\sigma_{\rm tide}} + \mathcal{A}_{\rm RD}(f) w^{+}_{\tilde{f}_{\rm RD}, d+\sigma_{\rm tide}}, \quad (15)$$

where $\mathcal{A}_{\rm RD}$ is given by Eq. (14).

The parameters entering Eqs. (14) and (15) are given by

$$\epsilon_{\rm tide} = 2 w^{+}_{x_1, d_1}(x_{\rm ND}), \quad (16)$$

where $x_1 = -0.0796251$, $d_1 = 0.0801192$, and

$$x_{\rm ND} \equiv \left(\frac{f_{\rm tide} - \tilde{f}_{\rm RD}}{\tilde{f}_{\rm RD}}\right)^2 - 0.571505\mathcal{C} - 0.00508451\chi; \quad (17)$$

$$\sigma_{\rm tide} = 2 w^{-}_{x_2, d_2}(x'_{\rm ND}), \quad (18)$$

where $x_2 = -0.206465$, $d_2 = 0.226844$ and

$$x'_{\rm ND} \equiv \left(\frac{f_{\rm tide} - \tilde{f}_{\rm RD}}{\tilde{f}_{\rm RD}}\right)^2 - 0.657424\mathcal{C} - 0.0259977\chi; \quad (19)$$

and finally

$$\delta'_2 = A w^{-}_{x_3, d_3}\left(\frac{f_{\rm tide} - \tilde{f}_{\rm RD}}{\tilde{f}_{\rm RD}}\right), \quad (20)$$

where $A = 1.62496$, $x_3 = 0.0188092$ and $d_3 = 0.338737$. Equation (16) slowly suppresses the ringdown of the BH remnant as the merger becomes less and less similar to the BH-BH case. We notice that, at variance with the nonspinning formulation of Paper I, we had to introduce two different independent variables for the two waveform parameters $\epsilon_{\rm tide}$ and $\sigma_{\rm tide}$, i.e. $x_{\rm ND} \neq x'_{\rm ND}$. Furthermore, the two independent variables now contain terms linear in χ. An example of nondisruptive merger spectrum is shown in the first panel in Fig. 1. Here, the hybrid waveform (in gray) is compared to the PhenomC model (dot-dashed blue), to the nonspinning NS-BH model of Paper I (dotted red), to the NS-BH model of [64] (dashed green), and to the model developed in this paper (long-dashed orange).

B. Disruptive mergers

If $f_{\rm tide} < f_{\rm RD}$ and $M_{\rm b,torus} > 0$, then the merger is disruptive, the NS material is scattered around the BH, and the ringdown contribution to Eq. (13) vanishes, i.e. $\epsilon_{\rm tide} = 0$ in Eq. (14). As in the case of nondisruptive mergers, the definition of this class is slightly different from its corresponding definition in Paper I. For disruptive mergers the waveform model reads

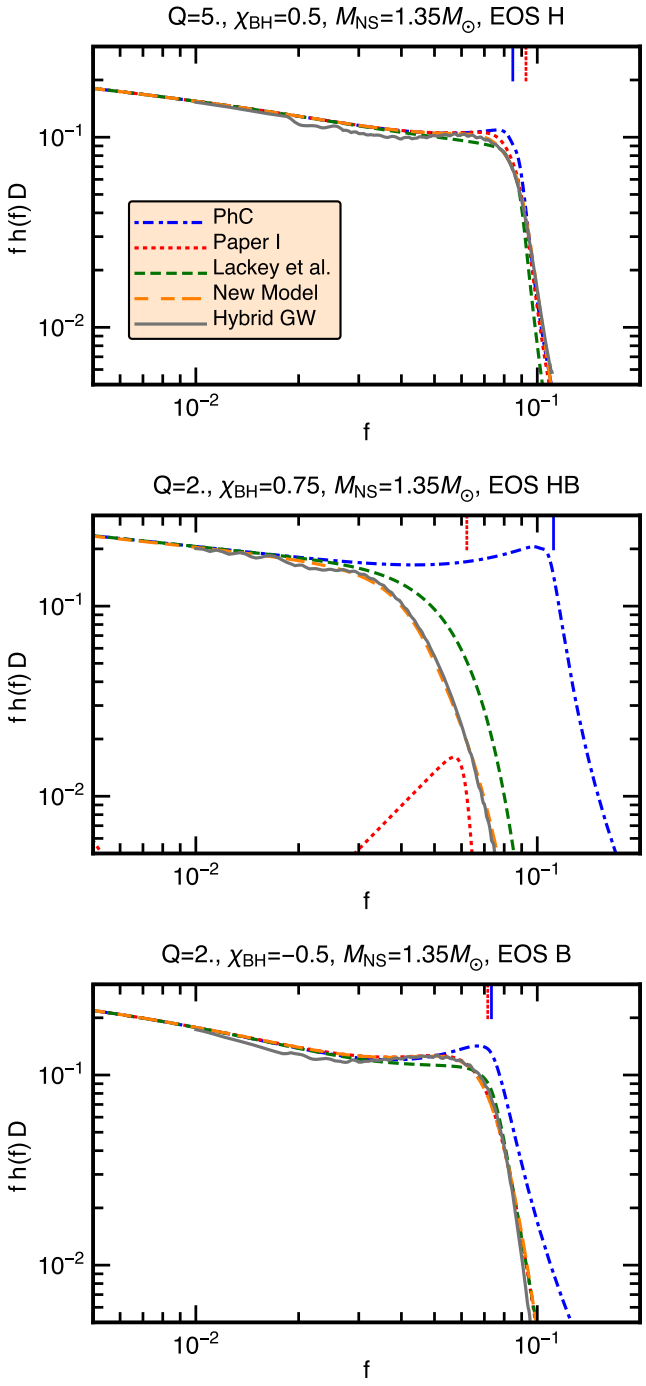

FIG. 1 (color online). Examples of nondisruptive, disruptive, and mildly disruptive merger waveforms (from top to bottom). The hybrid waveform (in gray) is compared to the PhenomC model (dot-dashed blue), to the nonspinning NS-BH model of Paper I (dotted red), to the NS-BH model of [64] (dashed green), and to the model developed in this paper (long-dashed orange). The short vertical lines denote $f_{\rm RD}$ and $f_{\rm tide}$ in blue and dotted red, respectively.

$$A_{\rm Phen}(f) = A_{\rm PN}(f) w^{-}_{\epsilon_{\rm ins} f_{\rm tide}, d+\sigma_{\rm tide}} + 1.25\gamma_1 f^{5/6} w^{-}_{f_{\rm tide}, d+\sigma_{\rm tide}}, \quad (21)$$

which is equivalent to Eq. (13) with $\tilde{f}_0 = f_{\rm tide}$ and $\epsilon_{\rm tide} = 0$. The remaining parameters to be prescribed are $\epsilon_{\rm ins}$ and $\sigma_{\rm tide}$. These are given by

$$\epsilon_{\rm ins} = a_1 + b_1 x_{\rm D}, \tag{22}$$

where $a_1 = 1.29971$, $b_1 = -1.61724$ and

$$x_{\rm D} \equiv \frac{M_{\rm b,torus}}{M_{\rm b,NS}} + 0.424912\mathcal{C} + 0.363604\sqrt{\nu} - 0.0605591\chi, \tag{23}$$

$\nu = M_{\rm NS}M_{\rm BH}/m_0^2$ being the symmetric mass ratio; and

$$\sigma_{\rm tide} = a_2 + b_2 x'_{\rm D}, \tag{24}$$

where $a_2 = 0.137722$, $b_2 = -0.293237$ and

$$x'_{\rm D} \equiv \frac{M_{\rm b,torus}}{M_{\rm b,NS}} - 0.132754\mathcal{C} + 0.576669\sqrt{\nu} - 0.0603749\chi - 0.0601185\chi^2 - 0.0729134\chi^3. \tag{25}$$

As in the case of nondisruptive mergers, two distinct definitions of the independent variable are used for the two waveform parameters, which was not the case in Paper I. Incidentally, this allows us to simplify the functional form of the parameter $\sigma_{\rm tide}$ with respect to Paper I. An example of disruptive merger spectrum is shown in the middle panel of Fig. 1. Notice that the nonspinning model of Paper I is completely inaccurate when high spin and strong tidal effects come into play, as the model did not account for the combination of the two.

C. Mildly disruptive mergers with no torus remnant

If $f_{\rm tide} < f_{\rm RD}$ and $M_{\rm b,torus} = 0$, then the merger is mildly disruptive, but *no* remnant torus is formed during the coalescence. The behavior of the GW amplitude for this class of mergers is captured by using the disruptive merger waveform model (Sec. IV B) and modifying two of its features. The first modification concerns the central frequencies of the windowing functions entering Eq. (21). In the present case we set

$$A_{\rm Phen}(f) = A_{\rm PN}(f) w^-_{f_1, d+\sigma_{\rm tide}} + 1.25\gamma_1 f^{5/6} w^-_{f_2, d+\sigma_{\rm tide}}, \tag{26}$$

where $f_1 = (1 - Q^{-1})\tilde{f}_{\rm RD} + Q^{-1}\epsilon_{\rm ins} f_{\rm tide}$ and $f_2 = (1 - Q^{-1})\tilde{f}_{\rm RD} + Q^{-1} f_{\rm tide}$ (our definition of the binary mass ratio is such that $Q \geq 1$). These two frequencies are introduced in order to obtain a smooth transition from nondisruptive to disruptive merger waveforms, which use $\tilde{f}_{\rm RD}$, and $\epsilon_{\rm ins} f_{\rm tide}$ and $f_{\rm tide}$ as windowing central frequencies, respectively. This constitutes a major improvement with respect to Paper I, where the low number of available nonspinning mildly disruptive simulations had not allowed us to go into such fine modeling details. Additionally, the scaling with Q is such that the model can accurately reproduce the data for mildly disruptive mergers with no torus remnant.

The second modification with respect to the disruptive merger waveform model in Eq. (21) is in the calculation of $\sigma_{\rm tide}$. For mildly disruptive mergers with no torus remnant, this calculation is performed by averaging the disruptive and the nondisruptive prescriptions; i.e., we evaluate Eqs. (18) and (24) and divide their sum by 2. As for f_1 and f_2, this modification allows for a smooth transition from disruptive to nondisruptive merger waveforms, and it is a notable improvement with respect to Paper I.

D. Mildly disruptive mergers with a torus remnant

If $f_{\rm tide} \geq f_{\rm RD}$ and $M_{\rm b,torus} > 0$, then the merger is mildly disruptive and a small remnant torus is produced. Mathematically, this class of mergers arises from a shortcoming of the approximations that lead to $f_{\rm tide}$, $M_{\rm b,torus}$, and, possibly, $f_{\rm RD}$: one would not expect a remnant torus to be formed if the system cannot reach the onset of tidal disruption. Physically, what the combination $f_{\rm tide} \geq f_{\rm RD}$ and $M_{\rm b,torus} > 0$ suggests (and what the hybrid waveforms that fall in these categories indeed show) is that some mildly disruptive mergers can achieve both a quasinormal mode (QNM) excitation of the BH remnant and the formation of a small remnant accretion torus.[4] From a phenomenological point of view this is to be expected, as the outer layers of the NS may be stripped to form the torus, while the core of the NS (or a fraction of it) may accrete onto the BH coherently enough to trigger the BH QNM oscillations (with regards to this topic, see Fig. 17 in [47] and our discussion of Fig. 6 below). We wish to remark that this level of sophistication in cataloging mildly disruptive mergers was not possible in Paper I, and is dictated by the fact that in the present work we have a larger catalog of numerical-relativity data to reproduce.

For mergers with $f_{\rm tide} \geq f_{\rm RD}$ and $M_{\rm b,torus} > 0$, the waveform amplitude model reads

$$A_{\rm Phen}(f) = A_{\rm PN}(f) w^-_{\epsilon_{\rm ins}\tilde{f}_{\rm RD}, d+\sigma_{\rm tide}} + 1.25\gamma_1 f^{5/6} w^-_{\epsilon_{\rm ins}\tilde{f}_{\rm RD}, d+\sigma_{\rm tide}} + \mathcal{A}_{\rm RD}(f) w^+_{\tilde{f}_{\rm RD}, d+\sigma_{\rm tide}}, \tag{27}$$

where $\epsilon_{\rm ins}$ is set according to Eq. (22), as for disruptive mergers, and $\sigma_{\rm tide}$ is given by Eq. (18), as for nondisruptive mergers. Notice that Eq. (27) resembles Eq. (15), with the

[4] $M_{\rm b,torus}$ was found to be $\leq 0.01 M_\odot$ for these tuning cases: this is clearly below the precision of Eq. (11).

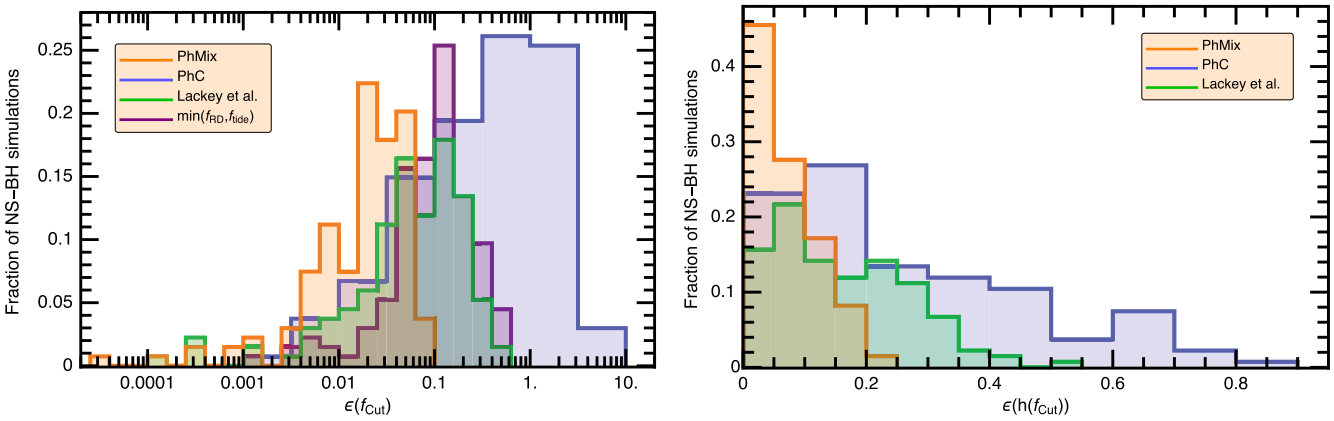

FIG. 2 (color online). Relative error distribution over the 134 NS-BH merger simulations for $f_{\rm cut}$ (left panel) and $h(f_{\rm cut})$ (right panel). All 134 results from the hybrid waveforms are compared to the predictions obtained from different models: the waveform model reported in this paper (PhMix, orange), PhenomC (PhC, blue), the waveform model of [64] (Lackey *et al.*, green), and the simple estimate given by $\min(f_{\rm RD}, f_{\rm tide})$ (purple). As discussed in the text this last proxy does not provide a waveform amplitude model, so it does not appear in the panel on the right.

exception of the use of $\epsilon_{\rm ins}$ in setting the first two windowing central frequencies: this allows for a smooth transition between nondisruptive and disruptive waveform models whenever the NS is tidally disrupted, but the excitation of the BH remnant ringdown takes place and no torus remnant is expected to survive the merger. An example of disruptive merger spectrum is shown in the last panel in Fig. 1; in this specific case, Eq. (27) is used to model the waveform amplitude.

V. TESTING THE WAVEFORM MODEL

Once the phenomenological NS-BH waveform amplitude model is formulated and calibrated via fits to hybrid waveforms built upon numerical-simulation data, its accuracy must be tested and demonstrated.

The qualitative behavior of the spinning waveform model is the same as for the nonspinning model formulated in Paper I. For the sake of brevity, we do not show all 134 GW spectra. We perform, instead, a quantitative assessment of the accuracy of the model in terms of two characteristic frequencies of each GW spectrum, $f_{\rm Max}$ and $f_{\rm cut}$, and the amplitude of each spectrum at these two frequencies. For the cutoff frequency $f_{\rm cut}$, we adopt the same, general definition introduced in Paper I, which also involves introducing and determining $f_{\rm Max}$. This definition has the advantage of allowing for a straightforward comparison among GW spectra originating from different models and/or calculations for the same binary, and for consistent comparisons among binaries with different physical parameters. The definition is as follows: $f_{\rm Max}$ is the frequency such that $f^2h(f)$ has a maximum, and $f_{\rm cut}$ is the frequency (greater than $f_{\rm Max}$) at which the amplitude drops by one e-fold, i.e.,

$$ef_{\rm cut}h(f_{\rm cut}) = f_{\rm Max}h(f_{\rm Max}). \tag{28}$$

We stress once more that this definition of the cutoff frequency is independent of the details of the waveform, and it works for any $h(f)$ (given in either analytical or numerical form).

Figures 2 and 3 show the distributions of the relative errors (ϵ) on $f_{\rm cut}$ and $h(f_{\rm cut})$, and $f_{\rm Max}$ and $h(f_{\rm Max})$, respectively. For each of the 134 hybrid waveforms, we determine these four quantities and compare them to the values predicted for them by several models. These are (1) the waveform model reported in this paper (labeled PhMix in the figures); (2) PhenomC (PhC); (3) the waveform model of [64] (Lackey *et al.*); and (4) the simple prescription $\min(f_{\rm RD}, f_{\rm tide})$, which, of course, cannot be used to predict $h(f_{\rm cut})$ and $h(f_{\rm Max})$, but just as a tentative proxy for $f_{\rm cut}$ and $f_{\rm Max}$. While the low frequency, inspiral regime is described by construction in the same way by all models, our new phenomenological model clearly introduces a considerable improvement in terms of accurately predicting all four high-frequency features of GWs emitted by spinning NS-BH coalescing binaries. Both the mean and maximum values of the $\epsilon(f_{\rm cut})$ and $\epsilon(f_{\rm Max})$ distributions are considerably reduced when using our model. The maximum relative error on the cutoff frequency is of order $\sim$10%, to be compared with $\sim$60% for the model of [64] and the proxy $\min(f_{\rm RD}, f_{\rm tide})$, and to even higher relative errors for PhenomC, which was not designed for NS-BH binaries. The simple prescription $\min(f_{\rm RD}, f_{\rm tide})$ is a better proxy for $f_{\rm cut}$ than it is for $f_{\rm Max}$. The advantages of our model are equally striking when considering $\epsilon(h(f_{\rm cut}))$ and $\epsilon(h(f_{\rm Max}))$. Both distributions are peaked at < 0.05 and fall off rapidly for the phenomenological NS-BH model, whereas this is not the case for PhenomC and the model of [64]. In conclusion, our approach is more accurate than all of these existing alternatives in modeling the GW spectra of NS-BH binaries.

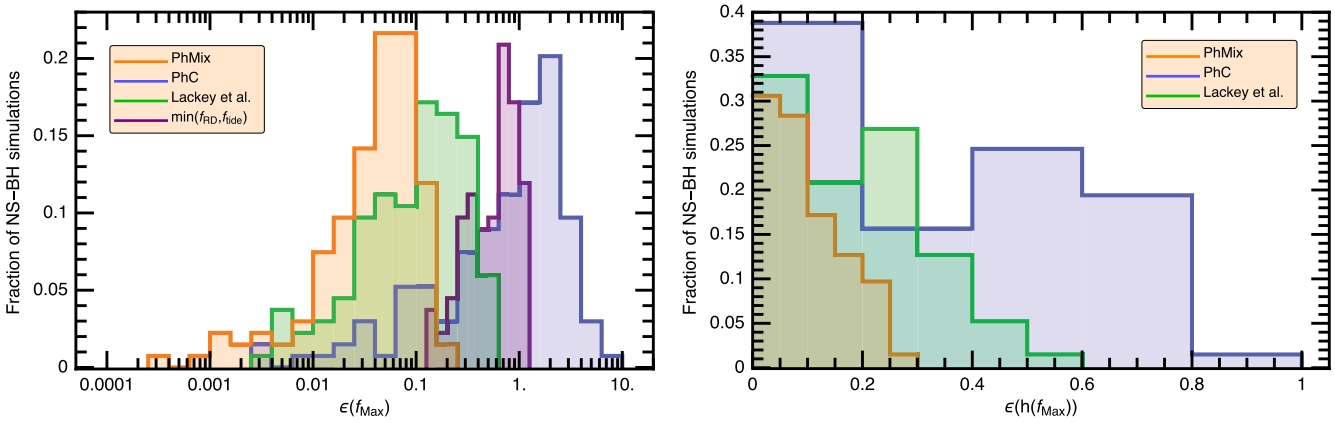

FIG. 3 (color online). Relative error distribution over the 134 NS-BH hybrid waveforms for $f_{\rm Max}$ (left panel) and $h(f_{\rm Max})$ (right panel). Colors and labeling are the same as in Fig. 2.

In Fig. 4 we separate the two contributions to the $\epsilon(f_{\rm cut})$ distribution shown in Fig. 2: in the left panel we show the distribution of the relative error on the cutoff frequency for the 59 binaries use to *calibrate* the model, while in the right panel we report the same distribution for the 75 binaries that were only used to *test* the model. A comparison with the left panel of Fig. 2 shows that the performance of our model is not dominated by results for calibration binaries. Analogous behaviors were obtained for $\epsilon(f_{\rm Max})$, $\epsilon(h(f_{\rm cut}))$ and $\epsilon(h(f_{\rm Max}))$.

VI. APPLICATIONS

A. The cutoff frequency

The panels in Fig. 5 show the cutoff frequency $f_{\rm cut}$ of nonspinning NS-BH binaries as a function of the NS mass $M_{\rm NS}$ and the binary mass ratio Q for the four different EOSs (2H, H, HB and B) used to compute the hybrid waveforms on which we built our phenomenological GW amplitude model. This figure is an updated version of Fig. 9 in Paper I. The contour line values are reported in hertz, with a 250 Hz spacing. The two dashed lines in each panel separate disruptive mergers (bottom left region), nondisruptive mergers (top right region), and mildly disruptive mergers (middle region in between the two lines). We remind the reader that disruptive mergers correspond to the conditions $f_{\rm tide} < f_{\rm RD}$ and $M_{\rm b,torus} > 0$; nondisruptive mergers are such that $f_{\rm tide} > f_{\rm RD}$ and $M_{\rm b,torus} = 0$; and mildly disruptive mergers do not fall into either of the previous categories. To help the reader, the three regions are explicitly indicated in the top left panel of the figure. In all panels, a green line marks the boundary between binaries with $M_{\rm b,torus} > 0$ and those with $M_{\rm b,torus} = 0$. Notice how these green lines overlap with the lower dashed lines: this indicates that the mildly disruptive mergers in these panels are such that the NS is tidally disrupted, but no remnant torus is formed. The main difference between these plots and those in Paper I is that the behavior of $f_{\rm cut}$ across the dashed transition lines is now smoother, and that the contours are continuous. This improvement over the original model is due to the larger data set used here, which allowed us to better tune our model in the mildly disruptive region.

The spin dependence of $f_{\rm cut}$ is illustrated in Fig. 6, where the different panels refer to initial BH spin parameters

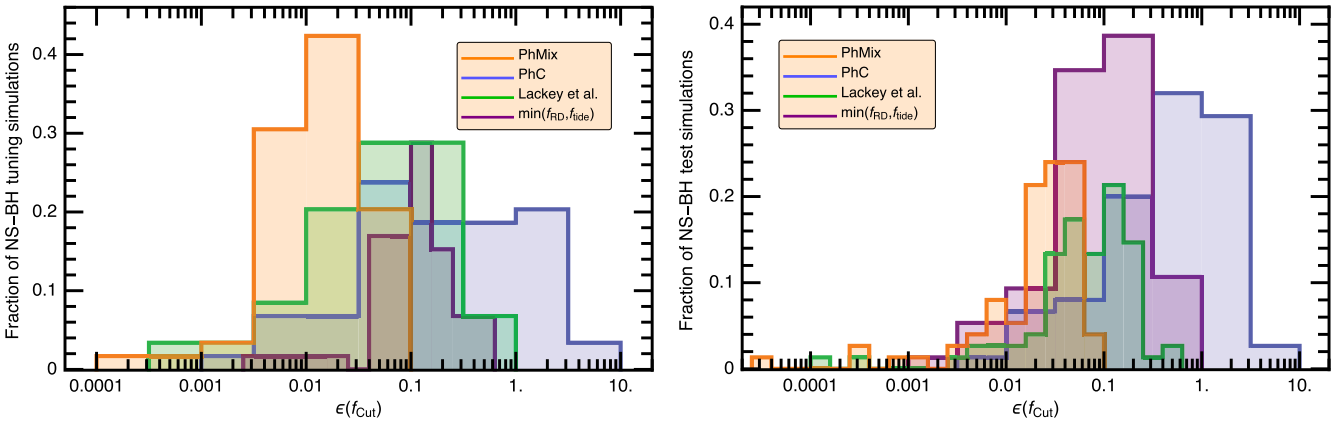

FIG. 4 (color online). Relative error distribution on $f_{\rm cut}$ (as in Fig. 2), but now the left panel refers to the 59 "calibration binaries" used to build the model, while the right panel refers to the 75 "test binaries" that were not used to build the model.

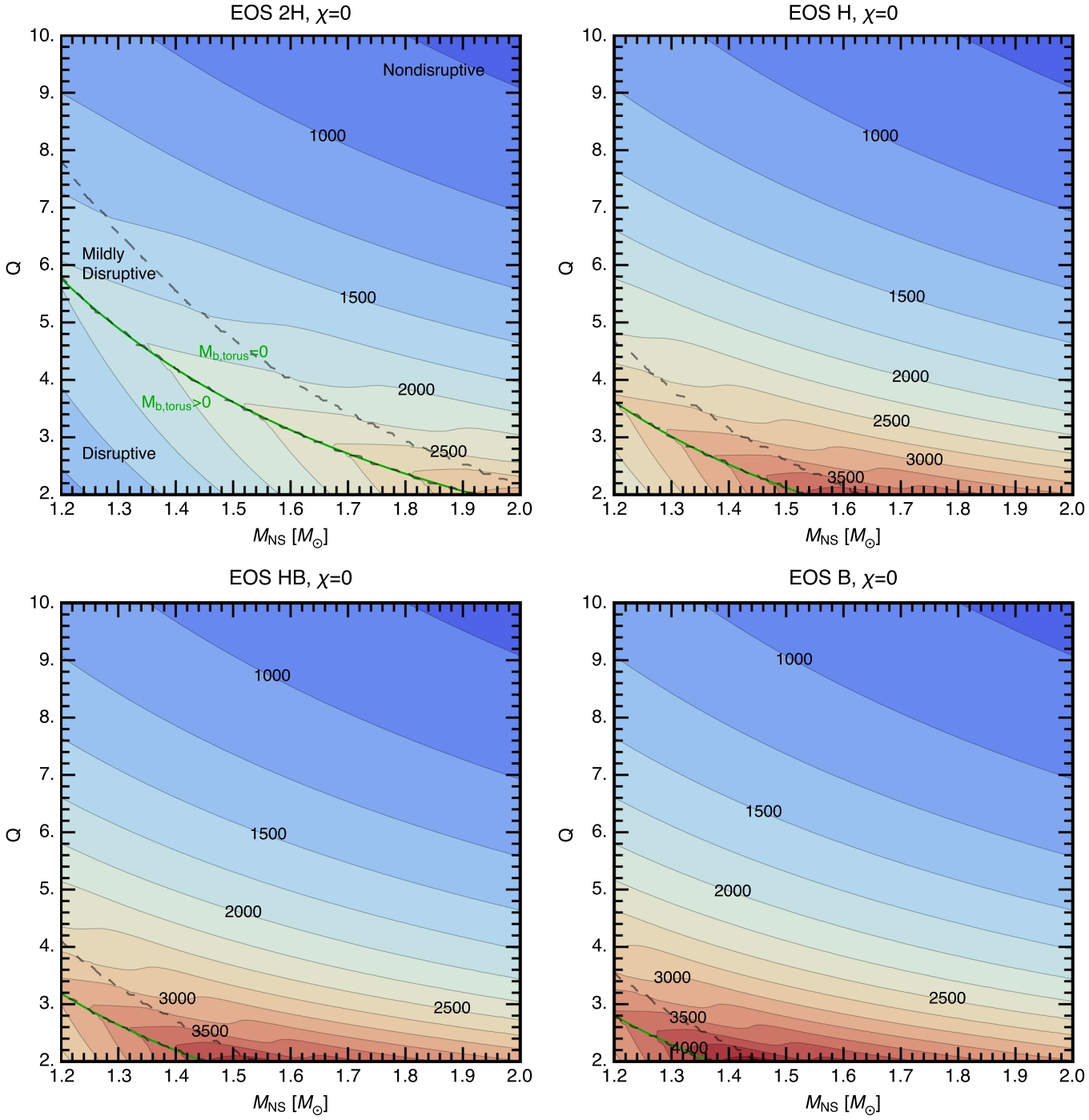

FIG. 5 (color online). The cutoff frequency $f_{\rm cut}$, as defined in Eq. (28), computed with our NS-BH GW amplitude model. We set the BH spin parameter χ to zero and consider the EOSs 2H, H, HB, B. The contour lines report $f_{\rm cut}$ in Hz and have a spacing of 250 Hz. The thick, green, continuous line is the location where $M_{\rm b,torus}$ vanishes, that is, where the left-hand side of Eq. (11) is zero. The dashed lines in each panel divide the plane in three regions, explicitly labeled only in the top right panel to avoid overcrowding the plots. These are a top right region in which the NS-BH coalescences are nondisruptive, i.e. $f_{\rm tide} \geq f_{\rm RD}$ and $M_{\rm b,torus} = 0$; a bottom left one in which they are disruptive, i.e. $f_{\rm tide} < f_{\rm RD}$ and $M_{\rm b,torus} > 0$; and a middle region in which mildly disruptive coalescences occur, i.e. $f_{\rm tide} < f_{\rm RD}$ and $M_{\rm b,torus} = 0$, or $f_{\rm tide} \geq f_{\rm RD}$ and $M_{\rm b,torus} > 0$. This figure should be compared to Fig. 9 of Paper I: notice how the contour lines and the transitions between different regimes are smoother with the new model we formulate in this paper.

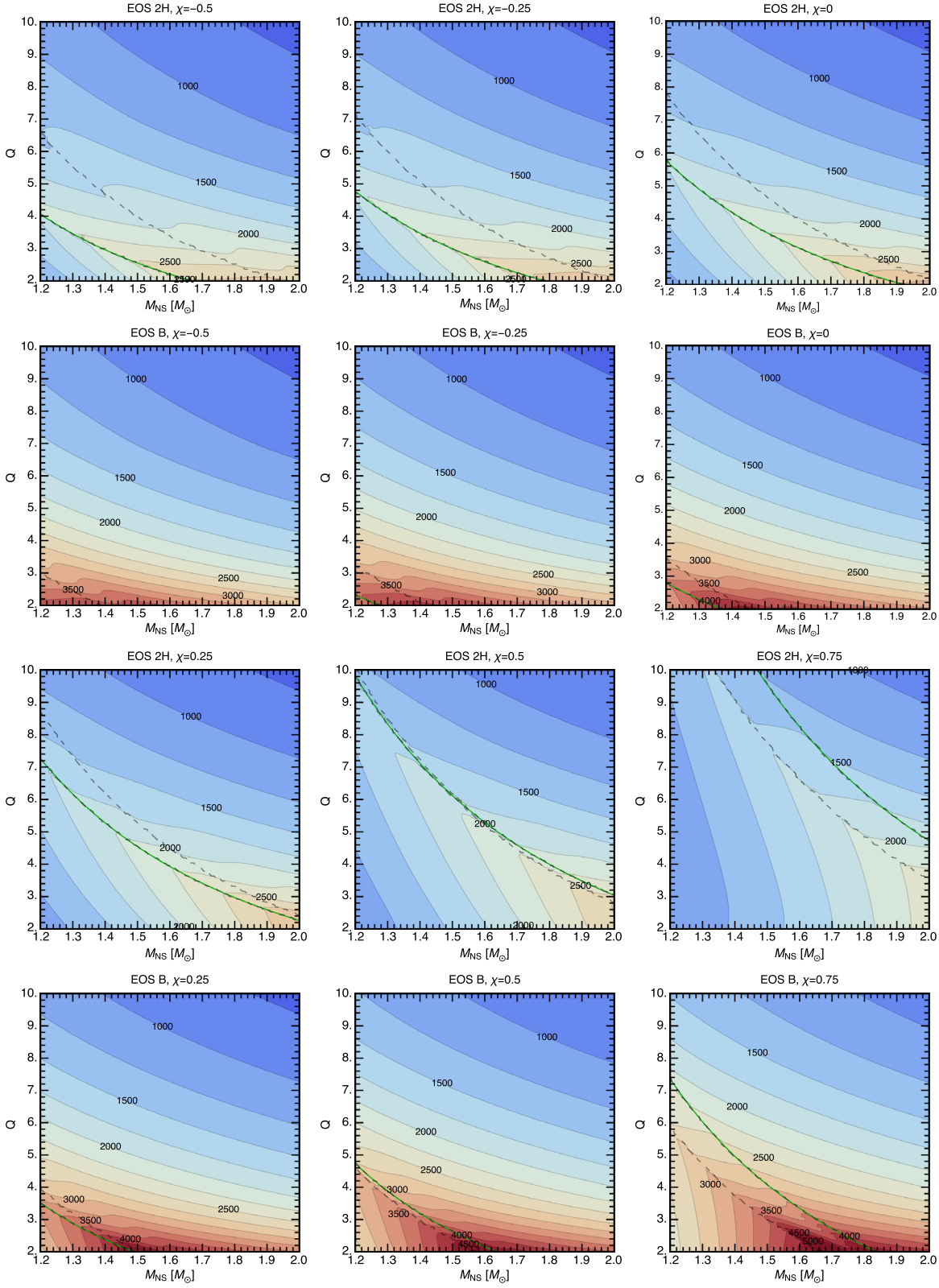

FIG. 6 (color online). The same as Fig. 5, but focusing only on the "extreme" EOSs 2H and B. The BH spins range between −0.5 and 0.75 in steps of 0.25, as indicated in each panel.

TABLE I. Values of the coefficients of the fits discussed in Eqs. (30) and (32). The number below each coefficient symbol must be multiplied by the power of 10 in square brackets on the right-hand side of the coefficient symbol. The g_{ijk}'s are reported in $G = c = m_0 = 1$ units.

b_{00} [10^1]	b_{10} [10^1]	b_{01} [10^1]	b_{20} [10^1]	b_{11} [10^1]	b_{02} [10^1]	b_{30} [10^0]	b_{21} [10^0]	b_{12} [10^0]	b_{03} [10^{-1}]
4.14730	−5.70783	2.57882	2.91134	−2.44263	1.04225	−5.26102	6.28215	−5.13944	3.99706
g_{000} [10^{-2}]	g_{100} [10^{-1}]	g_{010} [10^{-2}]	g_{001} [10^{-2}]	g_{200} [10^{-2}]	g_{020} [10^{-3}]	g_{002} [10^{-2}]	g_{110} [10^{-2}]	g_{101} [10^{-3}]	g_{011} [10^{-4}]
9.17677	−1.39031	−2.61399	2.43286	5.46375	1.74490	4.16418	2.31878	−7.49673	5.65265
g_{300} [10^{-3}]	g_{030} [10^{-5}]	g_{003} [10^{-3}]	g_{210} [10^{-3}]	g_{120} [10^{-4}]	g_{201} [10^{-4}]	g_{102} [10^{-2}]	g_{021} [10^{-4}]	g_{012} [10^{-3}]	g_{111} [10^{-3}]
−1.28721	−6.88240	−2.32757	3.64301	−4.05234	−8.98986	−1.87475	5.50808	−5.78858	−8.55090

$\chi \in \{-0.5, -0.25, 0, 0.25, 0.5, 0.75\}$ and we show two extreme cases for the EOS (2H and B). By comparing the EOS 2H and the EOS B panels, we therefore get an idea of the span of possible cutoff frequencies $f_{\rm cut}$ at a given BH spin value. As expected, the main differences occur in the disruptive merger regions, as this is where the NS EOS impacts the dynamical evolution of the binary. The relative size of the disruptive region grows with χ, because larger spins increase the likelihood of tidal disruption. It is interesting to notice that above $\chi \simeq 0.5$ the green torus mass boundary lines no longer track the lower dashed lines, but the upper ones (cf. the panels with $\chi = 0.75$, and the EOS B panel with $\chi = 0.5$). This means that a small remnant torus is likely to be formed for mildly disruptive mergers in these cases. It also demonstrates that there is indeed a need to split the phenomenological GW model into four subcases, as we do in this paper, at least until better analytical predictions are available for $M_{\rm b,torus}$, $f_{\rm tide}$, and $f_{\rm RD}$, if one wants to keep using these as tools to build the waveform model.

B. Phenomenological fits

As shown in a companion paper, the results presented above can be used to construct simple phenomenological formulas to determine (1) whether an NS-BH binary is disruptive, mildly disruptive, or nondisruptive; and (2) the GW cutoff frequency for disruptive mergers, due to the NS tidal disruption. Details are given in [80], and here we only review the main results.

1. Disruption criterion

The contours that separate NS-BH binaries with a disruptive fate from those with a mildly disruptive or nondisruptive fate in Figs. 5 and 6 may be fitted in several ways as a function of the physical parameters of the binary. The critical binary mass ratio $Q_{\rm D} = Q_{\rm D}(\mathcal{C}, \chi)$ below which mergers are disruptive is an approximately "universal" (i.e. EOS-independent) function that is well fitted by

$$Q_{\rm D} = \sum_{\substack{i,j=0 \\ i+j\leq 3}}^{3} a_{ij} \mathcal{C}^i \chi^j, \tag{29}$$

where the a_{ij}'s are constants (see [80] for details).

In building template banks for GW detection and for other applications, it may be useful to know $Q_{\rm D}$ as a function of the NS mass for NSs with large radii, as this is the case in which the GW emission from NS-BH systems differs the most from BH-BH binaries. A fit of the disruptive boundary for the 2H EOS yields

$$Q_{\rm D} = \sum_{\substack{i,j=0 \\ i+j\leq 3}}^{3} b_{ij} \bar{M}_{\rm NS}^i \chi^j, \tag{30}$$

where $\bar{M}_{\rm NS} = M_{\rm NS}/M_\odot$ and the coefficients take the values reported in Table I in units of $G = c = m_0 = 1$. We remark again that this fit gives a lower limit on $Q_{\rm D}$, as it was obtained using an exceptionally stiff EOS.

2. Cutoff frequency fitting formula

When tidal disruption occurs, as determined via Eq. (29), our phenomenological model allows us to determine a formula that provides the GW cutoff frequency analytically, as follows. We consider the 2H EOS, generate a set of 10^4 random disruptive mergers, compute $f_{\rm cut}$ for each NS-BH binary according to the definition in Eq. (28), and finally fit the data thus obtained. In order to select disruptive mergers, we randomly sample the parameter space in the ranges $M_{\rm NS}/M_\odot \in [1.2, 2.83]$ and $Q \in [2, 10]$, $\chi \in [-0.5, 0.75]$; we verify whether the sampled point corresponds to a disruptive binary, as defined just above Eq. (21), and keep the point if it does. The whole process is repeated until we have the desired set of 10^4 disruptive binaries. While the maximum NS mass for the 2H EOS is $\sim 2.83 M_\odot$, the maximum NS mass in our sample of disruptive NS-BH mergers is $\sim 2.28 M_\odot$. The resulting mass interval $M_{\rm NS}/M_\odot \in [1.2, 2.28]$ corresponds to the compactness interval $0.117 \leq \mathcal{C} \leq 0.221$. With this set of disruptive cutoff frequency data in hand, we fit $f_{\rm cut}$ in terms of the NS-BH binary parameters using the *ansatz*

$$f_{\rm cut} = \sum_{\substack{i,j=0 \\ i+j+k\leq 3}}^{3} f_{ijk} \mathcal{C}^i Q^j \chi^k, \tag{31}$$

where the fitting coefficients can be found in [80]. The relative error distribution for this fit with respect to the

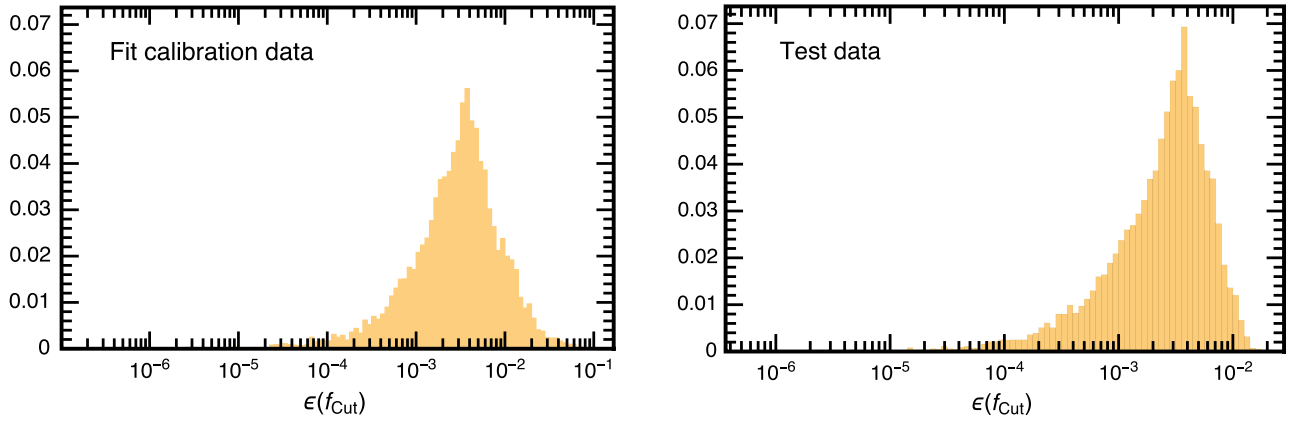

FIG. 7 (color online). Distribution of relative error on $f_{\rm cut}$ obtained by comparing the values given by the fit in Eq. (31) to the 10^4 EOS 2H data points used to produce the fit (left) and to 10^4 EOS B data points not involved in producing the fit (right).

original data points is shown in the left panel of Fig. 7. Notice that the peak of the distribution is below the percent level: the relative error for 68%, 95%, and 99.7% of the points is 0.47%, 1.5%, and 4.9%, respectively.

As a consistency check for this fitting formula, we draw a separate sample of 10^4 disruptive mergers, compute the GW amplitude cutoff frequency for each binary, and determine the relative errors of the fit just discussed against these test binaries. This time we use EOS B to construct our test sample and we lower the maximum allowed NS mass to $2M_\odot$, as this is approximately the maximum $M_{\rm NS}$ for this EOS. The compactness now ranges between ~0.161 and ~0.225. The result of this test is reported in the right panel of Fig. 7, where we show the relative error distribution for the fit in Eq. (31) with respect to the test set of binary mergers populated using EOS B. Remarkably, the maximum relative error is 2.2%, 97.6% of the points have a relative error that is smaller than 1%, and the peak of the distribution is once again below the percent level. The relative errors for the EOS B test set are even better than for the calibration set of EOS 2H, because EOS B covers a narrower range in compactness relative to EOS 2H. Furthermore, the fit of Eq. (31) is effectively EOS independent (or universal), at least within the parameter space region in which our model was calibrated.

For GW data analysis purposes, we also performed a fit of the 2H EOS $f_{\rm cut}$ data in terms of the NS mass, rather than its compactness:

$$f_{\rm cut} = \sum_{\substack{i,j=0 \\ i+j+k\leq 3}}^{3} g_{ijk} \bar{M}_{\rm NS}^i Q^j \chi^k, \tag{32}$$

where the coefficients g_{ijk} are listed in Table I. The resulting error distribution is similar to the one shown in the left panel of Fig. 7, but now the relative errors with respect to the EOS B test data are much higher than those in the right panel of Fig. 7 and range from 54% to 65%. In other words, the mass fit in Eq. (32) is *not* EOS universal. The fit is still useful, as it provides a lower limit to the GW amplitude cutoff frequency $f_{\rm cut}$ as a function of $M_{\rm NS}$, Q and χ.

VII. CONCLUSIONS

In this paper we have extended the phenomenological gravitational waveform amplitude model of Paper I to NS-BH binaries in which the BH has spin either aligned or antialigned with the orbital angular momentum. We have classified binaries in four broad categories: disruptive, nondisruptive, and mildly disruptive with and without a torus remnant.

The phenomenological tools developed in this paper can be used in various contexts, as detailed elsewhere [80]. Our predictions for the GW amplitude and for the cutoff frequency may be used to improve the template banks currently used in NS-BH searches, and they could also be exploited to build new NS-BH phenomenological GW phase models and EOB models. More accurate gravitational waveforms improve our chances of detecting GW signals and of extracting information from them. For example they could provide better constraints on the NS EOS [79,81] and possibly even on the underlying theory of gravity [82]. Furthermore, our work allows us to pinpoint binaries in which tidal effects are relevant. These cause the GW signal to deviate significantly from a BH-BH one and, possibly, lead to the emission of electromagnetic radiation. The latter may either be in the form of a relativistic jet launched by a hot, massive ($\gtrsim 0.01 M_\odot$) disk produced by the tidal disruption of the NS (a scenario that could explain the duration, energetics, and estimated event rates of SGRBs [83–85]), or in the form of isotropical radiation, i.e. macronovæ/kilonovæ, powered by decay heat of unstable r-process elements and by nonthermal radiation from electrons accelerated at blast waves between the merger ejecta and the interstellar medium [49,55,86–91]. For these reasons, our model can have an impact on

multimessenger searches targeting GW, electromagnetic, and neutrino radiation, as well as important applications in the interpretation of future multimessenger observations.

All our predictions are clearly affected by systematics in the initial data for the numerical simulations we used, in the numerical evolutions, in the phenomenological model itself and the tools it relies on [73,76], and in the fitting procedures. We expect these errors to increase when the model is extrapolated beyond the parameter space in which it was tuned. Future work should extend and improve our model in order to include not only the GW frequency domain amplitude, but also its phase. It should also consider larger values of the BH spin, nonzero NS spins and (most importantly) precession effects that occur when the BH spin is not aligned with the orbital angular momentum (see e.g. [48,62]). Further, any improvements in the underlying phenomenological BH-BH model can and should be included in our framework for NS-BH systems. In particular, the recent PhenomD BH-BH model [12,13] is calibrated to hybrid effective-one-body waveforms that use numerical-relativity simulations with mass ratios up to $1:18$, and BH dimensionless spin parameters up to ~ 0.85 (0.98 in the equal-mass case). This model is an improvement with respect to the PhenomC model, which was calibrated up to mass ratios of $1:4$, and resolves the technical limitations that may be encountered when using it for BH-BH systems with mass ratio higher than $1:20$ and $|\chi| > 0.9$. We plan to address all of these issues in the near future.

ACKNOWLEDGMENTS

This work was supported by STFC Grant No. ST/L000342/1, by the Japanese Grant-in-Aid for Scientific Research (Grants No. 21340051 and No. 24244028), and by the Grant-in-Aid for Scientific Research on Innovative Area (Grant No. 20105004). E. B. is supported by NSF CAREER Grant No. PHY-1055103 and by FCT Contract No. IF/00797/2014/CP1214/CT0012 under the IF2014 Programme. K. K. is supported by the RIKEN iTHES project. B. L. was supported by NSF Grants No. PHY-1305682, No. PHY-1205835, and No. AST-1333142. F. P. wishes to thank Alex Nielsen, Alessandra Buonanno, Stephen Fairhurst, Tanja Hinderer, and Bangalore Sathyaprakash for interesting discussions throughout the development of this work, along with Elena Pannarale for all her support.

[1] J. Aasi *et al.* (LIGO Scientific), Classical Quantum Gravity **32**, 074001 (2015).
[2] G. M. Harry (LIGO Scientific Collaboration), Classical Quantum Gravity **27**, 084006 (2010).
[3] F. Acernese *et al.* (VIRGO Collaboration), Classical Quantum Gravity **32**, 024001 (2015).
[4] K. Somiya (KAGRA Collaboration), Classical Quantum Gravity **29**, 124007 (2012).
[5] Y. Aso, Y. Michimura, K. Somiya, M. Ando, O. Miyakawa, T. Sekiguchi, D. Tatsumi, and H. Yamamoto, Phys. Rev. D **88**, 043007 (2013).
[6] IndIGO website, http://www.gw-indigo.org, 2012.
[7] P. Ajith, S. Babak, Y. Chen, M. Hewitson, B. Krishnan *et al.*, Classical Quantum Gravity **24**, S689 (2007).
[8] P. Ajith, S. Babak, Y. Chen, M. Hewitson, B. Krishnan *et al.*, Phys. Rev. D **77**, 104017 (2008).
[9] P. Ajith, Classical Quantum Gravity **25**, 114033 (2008).
[10] P. Ajith, M. Hannam, S. Husa, Y. Chen, B. Bruegmann *et al.*, Phys. Rev. Lett. **106**, 241101 (2011).
[11] L. Santamaría, F. Ohme, P. Ajith, B. Bruegmann, N. Dorband *et al.*, Phys. Rev. D **82**, 064016 (2010).
[12] S. Husa, S. Khan, M. Hannam, M. Pürrer, F. Ohme, X. Jiménez Forteza, and A. Bohé, arXiv:1508.07250.
[13] S. Khan, S. Husa, M. Hannam, F. Ohme, M. Pürrer, X. Jiménez Forteza, and A. Bohé, arXiv:1508.07253.
[14] M. Hannam, P. Schmidt, A. Bohé, L. Haegel, S. Husa, F. Ohme, G. Pratten, and M. Pürrer, Phys. Rev. Lett. **113**, 151101 (2014).
[15] A. Taracchini, Y. Pan, A. Buonanno, E. Barausse, M. Boyle, T. Chu, G. Lovelace, H. P. Pfeiffer, and M. A. Scheel, Phys. Rev. D **86**, 024011 (2012).
[16] T. Damour, A. Nagar, and S. Bernuzzi, Phys. Rev. D **87**, 084035 (2013).
[17] T. Damour, A. Nagar, and M. Trias, Phys. Rev. D **83**, 024006 (2011).
[18] F. Ohme, M. Hannam, and S. Husa, Phys. Rev. D **84**, 064029 (2011).
[19] Y. Pan, A. Buonanno, A. Taracchini, L. E. Kidder, A. H. Mroué, H. P. Pfeiffer, M. A. Scheel, and B. Szilágyi, Phys. Rev. D **89**, 084006 (2014).
[20] A. Taracchini *et al.*, Phys. Rev. D **89**, 061502 (2014).
[21] B. Szilágyi, J. Blackman, A. Buonanno, A. Taracchini, H. P. Pfeiffer, M. A. Scheel, T. Chu, L. E. Kidder, and Y. Pan, Phys. Rev. Lett. **115**, 031102 (2015).
[22] D. A. Brown, P. Kumar, and A. H. Nitz, Phys. Rev. D **87**, 082004 (2013).
[23] I. W. Harry, A. H. Nitz, D. A. Brown, A. P. Lundgren, E. Ochsner, and D. Keppel, Phys. Rev. D **89**, 024010 (2014).
[24] B. Aylott, J. G. Baker, W. D. Boggs, M. Boyle, P. R. Brady *et al.*, Classical Quantum Gravity **26**, 165008 (2009).
[25] P. Ajith, M. Boyle, D. A. Brown, B. Brugmann, L. T. Buchman *et al.*, Classical Quantum Gravity **29**, 124001 (2012).
[26] I. Hinder, A. Buonanno, M. Boyle, Z. B. Etienne, J. Healy *et al.*, Classical Quantum Gravity **31**, 025012 (2013).
[27] P. Ajith and S. Bose, Phys. Rev. D **79**, 084032 (2009).

[28] F. Ohme, A. B. Nielsen, D. Keppel, and A. Lundgren, Phys. Rev. D **88**, 042002 (2013).
[29] J. Abadie *et al.* (LIGO Scientific Collaboration, Virgo Collaboration), Classical Quantum Gravity **27**, 173001 (2010).
[30] S. Marassi, R. Schneider, G. Corvino, V. Ferrari, and S. Portegies Zwart, Phys. Rev. D **84**, 124037 (2011).
[31] X.-J. Zhu, E. J. Howell, D. G. Blair, and Z.-H. Zhu, Mon. Not. R. Astron. Soc. **431**, 882 (2013).
[32] M. Dominik, E. Berti, R. O'Shaughnessy, I. Mandel, K. Belczynski, C. Fryer, D. Holz, T. Bulik, and F. Pannarale, Astrophys. J. **806**, 263 (2015).
[33] Y. Sekiguchi, K. Kiuchi, K. Kyutoku, and M. Shibata, Phys. Rev. Lett. **107**, 211101 (2011).
[34] K. Hotokezaka, K. Kyutoku, H. Okawa, M. Shibata, and K. Kiuchi, Phys. Rev. D **83**, 124008 (2011).
[35] K. Hotokezaka, K. Kiuchi, K. Kyutoku, H. Okawa, Y.-i. Sekiguchi, M. Shibata, and K. Taniguchi, Phys. Rev. D **87**, 024001 (2013).
[36] S. Bernuzzi, A. Nagar, T. Dietrich, and T. Damour, Phys. Rev. Lett. **114**, 161103 (2015).
[37] A. Bauswein and N. Stergioulas, Phys. Rev. D **91**, 124056 (2015).
[38] S. Bernuzzi, T. Dietrich, and A. Nagar, Phys. Rev. Lett. **115**, 091101 (2015).
[39] A. Buonanno, B. Iyer, E. Ochsner, Y. Pan, and B. Sathyaprakash, Phys. Rev. D **80**, 084043 (2009).
[40] E. Berti, S. Iyer, and C. M. Will, Phys. Rev. D **77**, 024019 (2008).
[41] K. Kyutoku, M. Shibata, and K. Taniguchi, Phys. Rev. D **79**, 124018 (2009).
[42] K. Kyutoku, M. Shibata, and K. Taniguchi, Phys. Rev. D **90**, 064006 (2014).
[43] F. Foucart, L. E. Kidder, H. P. Pfeiffer, and S. A. Teukolsky, Phys. Rev. D **77**, 124051 (2008).
[44] K. Henriksson, F. Foucart, L. E. Kidder, and S. A. Teukolsky, arXiv:1409.7159.
[45] M. Shibata, K. Kyutoku, T. Yamamoto, and K. Taniguchi, Phys. Rev. D **79**, 044030 (2009).
[46] K. Kyutoku, M. Shibata, and K. Taniguchi, Phys. Rev. D **82**, 044049 (2010).
[47] K. Kyutoku, H. Okawa, M. Shibata, and K. Taniguchi, Phys. Rev. D **84**, 064018 (2011).
[48] F. Foucart, M. B. Deaton, M. D. Duez, L. E. Kidder, I. MacDonald, C. D. Ott, H. Pfeiffer, M. Scheel, B. Szilagyi, and S. Teukolsky, Phys. Rev. D **87**, 084006 (2013).
[49] K. Kyutoku, K. Ioka, and M. Shibata, Phys. Rev. D **88**, 041503 (2013).
[50] F. Foucart, L. Buchman, M. D. Duez, M. Grudich, L. E. Kidder, I. MacDonald, A. Mroue, H. P. Pfeiffer, M. A. Scheel, and B. Szilagyi, Phys. Rev. D **88**, 064017 (2013).
[51] M. B. Deaton, M. D. Duez, F. Foucart, E. O'Connor, C. D. Ott, L. E. Kidder, C. D. Muhlberger, M. A. Scheel, and B. Szilagyi, Astrophys. J. **776**, 47 (2013).
[52] M. Tanaka, K. Hotokezaka, K. Kyutoku, S. Wanajo, K. Kiuchi, Y. Sekiguchi, and M. Shibata, Astrophys. J. **780**, 31 (2014).
[53] F. Foucart, M. B. Deaton, M. D. Duez, E. O'Connor, C. D. Ott, R. Haas, L. E. Kidder, H. P. Pfeiffer, M. A. Scheel, and B. Szilagyi, Phys. Rev. D **90**, 024026 (2014).
[54] F. Foucart, E. O'Connor, L. Roberts, M. D. Duez, R. Haas, L. E. Kidder, C. D. Ott, H. P. Pfeiffer, M. A. Scheel, and B. Szilagyi, Phys. Rev. D **91**, 124021 (2015).
[55] K. Kyutoku, K. Ioka, H. Okawa, M. Shibata, and K. Taniguchi, Phys. Rev. D **92**, 044028 (2015).
[56] Z. B. Etienne, Y. T. Liu, S. L. Shapiro, and T. W. Baumgarte, Phys. Rev. D **79**, 044024 (2009).
[57] M. D. Duez, F. Foucart, L. E. Kidder, C. D. Ott, and S. A. Teukolsky, Classical Quantum Gravity **27**, 114106 (2010).
[58] Z. B. Etienne, Y. T. Liu, V. Paschalidis, and S. L. Shapiro, Phys. Rev. D **85**, 064029 (2012).
[59] Z. B. Etienne, V. Paschalidis, and S. L. Shapiro, Phys. Rev. D **86**, 084026 (2012).
[60] G. Lovelace, M. D. Duez, F. Foucart, L. E. Kidder, H. P. Pfeiffer, M. A. Scheel, and B. Szilágyi, Classical Quantum Gravity **30**, 135004 (2013).
[61] V. Paschalidis, Z. B. Etienne, and S. L. Shapiro, Phys. Rev. D **88**, 021504 (2013).
[62] K. Kawaguchi, K. Kyutoku, H. Nakano, H. Okawa, M. Shibata, and K. Taniguchi, Phys. Rev. D **92**, 024014 (2015).
[63] K. Kiuchi, Y. Sekiguchi, K. Kyutoku, M. Shibata, K. Taniguchi, and T. Wada, arXiv:1506.06811.
[64] B. D. Lackey, K. Kyutoku, M. Shibata, P. R. Brady, and J. L. Friedman, Phys. Rev. D **89**, 043009 (2014).
[65] T. Yamamoto, M. Shibata, and K. Taniguchi, Phys. Rev. D **78**, 064054 (2008).
[66] F. Pannarale, E. Berti, K. Kyutoku, and M. Shibata, Phys. Rev. D **88**, 084011 (2013).
[67] M. Hannam, S. Husa, F. Ohme, and P. Ajith, Phys. Rev. D **82**, 124052 (2010).
[68] LORENE website, http://www.lorene.obspm.fr.
[69] K. Kyutoku, M. Shibata, and K. Taniguchi, Phys. Rev. D **79**, 124018 (2009).
[70] C. Reisswig and D. Pollney, Classical Quantum Gravity **28**, 195015 (2011).
[71] B. D. Lackey, K. Kyutoku, M. Shibata, P. R. Brady, and J. L. Friedman, Phys. Rev. D **85**, 044061 (2012).
[72] J. S. Read, B. D. Lackey, B. J. Owen, and J. L. Friedman, Phys. Rev. D **79**, 124032 (2009).
[73] F. Pannarale, Phys. Rev. D **88**, 104025 (2013).
[74] F. Pannarale, Phys. Rev. D **89**, 044045 (2014).
[75] E. Berti, V. Cardoso, and C. M. Will, Phys. Rev. D **73**, 064030 (2006).
[76] F. Foucart, Phys. Rev. D **86**, 124007 (2012).
[77] J. M. Bardeen, W. H. Press, and S. A. Teukolsky, Astrophys. J. **178**, 347 (1972).
[78] L. Rezzolla, P. Diener, E. N. Dorband, D. Pollney, C. Reisswig, E. Schnetter, and J. Seiler, Astrophys. J. **674**, L29 (2008).
[79] F. Pannarale, L. Rezzolla, F. Ohme, and J. S. Read, Phys. Rev. D **84**, 104017 (2011).
[80] F. Pannarale, E. Berti, K. Kyutoku, B. D. Lackey, and M. Shibata, arXiv:1509.06209.
[81] J. S. Read, C. Markakis, M. Shibata, K. Uryu, J. D. Creighton, and J. Friedman, Phys. Rev. D **79**, 124033 (2009).
[82] E. Berti *et al.*, arXiv:1501.07274.
[83] B. Paczynski, Acta Astron. **41**, 257 (1991).
[84] E. Nakar, Phys. Rep. **442**, 166 (2007).
[85] E. Berger, Annu. Rev. Astron. Astrophys. **52**, 43 (2014).

[86] L.-X. Li and B. Paczyński, Astrophys. J. **507**, L59 (1998).
[87] S. R. Kulkarni, arXiv:astro-ph/0510256.
[88] B. D. Metzger G. Martínez-Pinedo, S. Darbha, E. Quataert, A. Arcones, D. Kasen, R. Thomas, P. Nugent, I. V. Panov, and N. T. Zinner, Mon. Not. R. Astron. Soc. **406**, 2650 (2010).
[89] E. Nakar and T. Piran, Nature (London) **478**, 82 (2011).
[90] S. Kisaka, K. Ioka, and H. Takami, Astrophys. J. **802**, 119 (2015).
[91] B. Yang, Z.-P. Jin, X. Li, S. Covino, X.-Z. Zheng, K. Hotokezaka, Y.-Z. Fan, T. Piran, and D.-M. Wei, Nat. Commun. **6**, 7323 (2015).